Asymmetric phase diagram and dimensional crossover in a system of spin* dimers under applied hydrostatic pressure

M. J. Coak,[1,2,3] S. P. M. curley,[1] Z. Hawkhead0,[4] J. P. Tideyo,[5] D. Graf,[6] S. J. Clark,[4] P. Senguptao 7
Z. E. Manson,[8] T. LancasterD,[4] P. A. Goddard,[1,*] and J. L. Manson[8,†]
Department of Physics, University of Warwick, Gibbet Hill Road, Coventry CV4 7AL, United Kingdom
[2]London Centrefor Nanotechnology, University College Inndon, Gordon St., Inndon WCIH OAH, United Kingdom
[3] School ofPhysics and Astronomy, University of Birmingham, Edgbaston, Birmingham B15 277t United Kingdom
[4]Department of Physics, Centre for Materials Physics, Durham University, Durham DHI 3LE, United Kingdom
[5]Department ofChemistry, University of Wamick, Gibbet Hill, Coventry CV4 7AL United Kingdom
('National High Magnetic Field Laboratory, Florida State University, Tallahassee, Florida 32310, USA
[7]School of Physical and Mathematical Sciences, Nanyang Technological University, 21 Nanyang Link, 637371 Singapore
[8]Department ofChemistry and Biochemistry, Eastern Washington University, Cheney, Washington 99004, USA

8) (Received 23 August 2023; revised 11 November 2023; accepted 13 November 2023; published 26 December 2023)

We present the magnetic and structural properties of $Cu(pyrazine)_{0.5}(glycine)]ClO_4$ under applied pressure. As previously reported, at ambient pressure this material consists of quasi-two-dimensional layers of weakly coupled antiferromagnetic dimers which undergo Bose-Einstein condensation of triplet excitations between two magnetic field-induced quantum critical points (QCPs). The molecular building blocks from which the compound is constructed give rise to exchange strengths that are considerably lower than those found in other S = 1/2 dimer materials, which allows us to determine the pressure evolution of the entire field-temperature magnetic phase diagram using radio-frequency magnetometry. We find that a distinct phase emerges above the upper field-induced transition at elevated pressures and also show that an additional QCP is induced at zero field at a critical pressure of pc = 15.7(5) kbar. Pressure-dependent single-crystal x-ray diffraction and density functional theory calculations indicate that this QCP arises primarily from a dimensional crossover driven by an increase in the interdimer interactions between the planes. While the effect of quantum fluctuations on the lower field-induced transition is enhanced with applied pressure, quantum Monte Carlo calculations suggest that this alone cannot explain an unconventional asymmetry that develops in the phase diagram.

DOI: 10.1103/PhysRevB.108.224431

1. INTRODUCTION

Low-dimensional, low-spin magnetic materials in an applied magnetic field provide an unparalleled solid-state experimental testing ground for fundamental quantum phenomena, including the effects of zero-point fluctuations and quantum phase transitions [1—5]. In particular, the weakly coupled S 1/2 antiferromagnetic (AFM) dimer system has been extensively studied and is known to exhibit a quantum disordered state, as well as Bose-Einstein condensation of triplet excitations that occurs between two field-induced quantum critical points (QCPs) [6]. In principle, an additional QCP distinct from that manifested by applied field can be reached by enhancing the intradimer magnetic interactions using hydrostatic pressure [7]. This has been achieved in a few cases, however, bulk magnetometry measurements are difficult to perform under high pressure and the energy scales in the materials studied so far have limited the scope of the appliedpressure measurements to only a portion of the magnetic phase diagram. Here we report magnetometry measurements at pressures up to 22 kbar on a quasi-two-dimensional (Q2D) $S = 1/2$ dimer material across a field and temperature range that spans the full magnetic phase diagram. The magnetometry results are discussed in light of pressure-dependent x-ray diffraction and density functional theory (DFT), as well as quantum Monte Carlo (QMC) calculations.

At low temperatures and zero magnetic field, weakly interacting Heisenberg S 1/2 AFM dimers are found in a state of quantum disorder, in which zero-point fluctuations abound

*p.goddard@warwick.ac.u
k tDeceased.

[6]. The dimers are arranged as S 0 singlets separated in energy from an excited degenerate S 1 triplet state by an energy gap determined by the intradimer exchange energy Jo (see Fig. 1). Exchange pathways between dimers will give rise to an effective interdimer interaction J' that acts to disperse the excited triplet, leading to a band of excitations. Turning on a magnetic field, the triplet states will split until the exchange broadened Sz = +1 state crosses the singlet state at the Hcl QCP and long-range X Y-AFM order is established. Increasing the field further eventually realizes a fully field-aligned

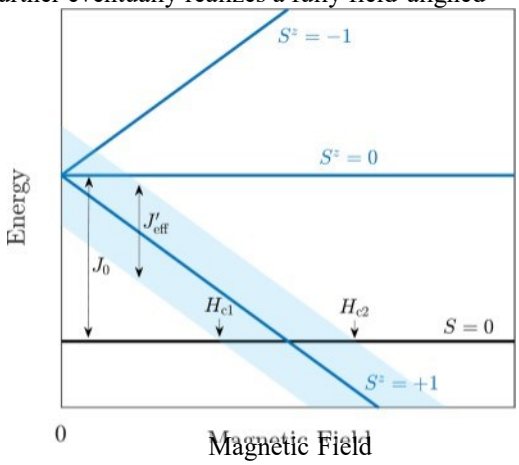

FIG. 1. Schematic energy level diagram for weakly coupled S = 1/2 AFM dimers in a magnetic field.

state at the Hc2 QCP. The situation can be thought of as a nonmagnetic vacuum from which emerge spin-I bosonic excitations (triplets), which increase in number as field is swept, spontaneously break SO(2) symmetry to form a condensate at (provided the spin Hamiltonian itself maintains this symmetry) and reach saturation at Hc2.

The singlet-triplet gap can also be closed by tuning Jo and/or Jeff via application of pressure in the absence of a symmetry-breaking magnetic field. This QCP occurs at a pressure pc, beyond which long-range order develops that now spontaneously breaks SO(3) symmetry While several dimer systems have been shown to exhibit a reduction in the gap with pressure, in only a few compounds has it been possible to suppress the QCP completely to zero field, namely, TICuC13 KCuC13 [9], and (C4H12N2)Cu2C16 (PHCC) [10,111 with pc I, 8, and 4 kbar, respectively. All these materials possess large Hc2 values beyond the range of superconducting magnets (æ100 T for TICuC13', 55 T for KCuC13; and 37 T for PHCC at ambient pressure, see Ref. [6] and references therein), which has limited previous pressure studies to the low-field portion of the phase diagram.

Here we study the Q2D S 1/2 dimer system (pyz pyrazine C4H4N2; gly =glycine C2H5N02) [12, 13] which, thanks to the reduced magnetic energy scales manifested in molecule-based quantum magnets, has a uniquely accessible ambient pressure Hc2 close to 6 T. Using a radio-frequency technique, we are able to perform direct magnetometry measurements that encompass both field-induced QCPs up to and beyond the critical pressure of 15.7(5) kbar. In this way, we have found that the effect of quantum fluctuations on the low-field QCP is strongly enhanced as it is suppressed to lower fields while the high-field QCP remains largely unaffected. We also find that an additional, possibly canted, magnetic phase develops above Hc2 at high pressures.

Furthermore, by performing detailed structural and DFT studies under pressure and comparing our results to QMC simulations, we deduce that the pressure-induced quantum phase transition is primarily driven by an interlayer interdimer interaction that grows with pressure while the intradimer coupling remains roughly constant, eventually causing a crossover from two- to three-dimensional magnetism. An asymmetry develops in the H-T phase diagram as pressure increases, likely arising from a subtle field dependence of the secondary magnetic interactions.

Below, after introducing the material in question and describing the experimental methods, we present the magnetometry, x-ray diffraction and DFT data. All the results are compared and their implications considered in the Discussion section.

$[Cu(pyz)_{0.5}(gly)]ClO_4$

$[Cu(pyz)_{0.5}(gly)]ClO_4$ crystalizes into crystalizes into a monoclinic structure with space group P21 /n (see Fig. 2) [12, 13]. The material is based on a lattice of weakly interacting S = 1/2 dimers, with the dimer-unit itself composed of two Cu ions linked by a bridging pyz molecule which mediates the primary intradimer exchange interaction (JD. The Cu-pyz-Cu dimer-unit is indicated in Fig. 2 with shaded regions.

As described in detail in Refs. [12,131, glycine ligands mediate the primary interdimer exchange (J' I) and bridge each dimer to four nearest dimer neighbors. dimers are arranged in corrugated sheets which stack along the [JOT] direction. The sheets are separated by C104 counter ions, which bond to the dimer along the Jahn-TeIIer axis of the Cu. Due to this, the dx2_y2 orbitals on the Cu sites lie within the equatorial Cu02N2 plane, such that at ambient pressure the Cu • • • • • • Cu coordination bond mediates only very weak secondary interdimer exchange (Jé104) between the layers, as shown in Fig. 2(b).

As a result of this structure, $Cu(pyz)_{0.5}(gly)]ClO_4$ can be modeled as a lattice of weakly coupled S = 1/2 AFM dimers interacting via Heisenberg exchange, with the magnetic properties summarized by

$$\mathcal{H} = J_0 \sum_i \hat{\mathbf{S}}_{1,i} \cdot \hat{\mathbf{S}}_{2,i} \qquad + {}^{J}\mathrm{AY\,E}\hat{\mathbf{S}}_{m,i} \cdot \hat{\mathbf{S}} \quad (\mathrm{mnij})\ \mathrm{Il}$$

$$+ J''_{\mathrm{ClO_4}} \sum_{\langle mnij\rangle\perp} \hat{\mathbf{S}} \qquad \mathrm{Sm,i} \bullet \mathrm{Sn,j} - \mathfrak{z}\mu_B\mu_0 H \rangle \; S^{\kappa}_{m.i}\cdot(\mathrm{l})$$

where i and j denote dimers and m, n 1, 2 label magnetic sites within a dimer. The first term represents the intradimer interaction, while the second and third terms are the interdimer interactions between neighboring dimers within and perpendicular to the corrugated sheets, respectively. The structure also allows for an additional Dzyaloshinskii-Moriya (DM) interaction term in the Hamiltonian of the form D • (Sl x S2), but no effects of such a perturbation have so far been detected in the temperature ranges measured and the effective spin model relevant to the experiments retains SO(2) symmetry, at least at ambient pressure [13].

Previous data showed the expected lack of long-range ordering down to T 32 mK at zero field, the existence of two field-induced QCPs (determined from magnetization, muon spin rotation, and heat capacity measurements), and a H-T phase diagram consistent with other S = 1/2 dimer materials [12,14]. Reference [13] found that 5.8(3) K and J'gly= 1.6(1) K, while J" C104 is small but nonzero, with the system being well described as Q2D network of dimers with AFM

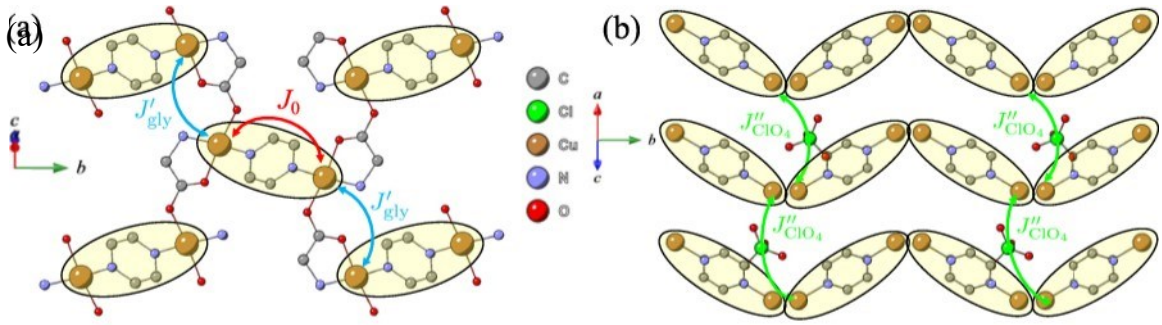

FIG. 2. Ambient pressure crystal structure of $[Cu(pyz)_{0.5}(gly)]ClO_4$ measured at 300 K with dimer units denoted by shaded reg measured at 300 K with dimer units denoted by shaded regions. Each unit cell contains four formula units, which correspond to two complete dimer units. (a) View along the [IOTI direction showing corrugated dimer sheets with intradimer (JD and interdimer (J'gly) exchange pathways marked with arrows. (b) View along the [1011 direction showing three layers of the corrugated dimer sheets and the interlayer exchange (J'é104) pathway between Cu(ll) ions via C104 molecules. Adjacent dimers in each layer are connected by the glycine molecules that extend into the page, as shown in (a).

coupling between the dimers. This is further supported by our DEI' calculations discussed below.

11. METHODS

A. Synthesis

Single crystal samples of $Cu(pyz)_{0.5}(gly)]ClO_4$ were prepared according to the procedure established in Ref. [12] (and the supporting information therein).

B. Crystal structure determination

The blue crystal of dimensions 0.26 x 0.24 x 0.10 mm was loaded into an Almax-EasyLab Diacell TozerDAC alongside a ruby chip standard for pressure measurement [15]. The cell employed a preindented steel gasket of 150 gm thickness with a 500 um diameter hole mechanically drilled to form the sample chamber. 4:1 MeOH/EtOH (nondried) solution was used as the pressure-transmitting medium. Data were collected at 0.5, 3.9, 7.4, 9.8, 15.5, 17.9, 21.4, 23.1, 26.6, and 28.2 kbar on a Rigaku Oxford Diffraction SuperNova diffractometer employing mirror monochromated MO Ka radiation from a microfocus source detected at an AtlasS2 CCD area detector. Uncertainty on these pressure values was estimated at ± 1 kbar from the ruby spectroscopy linewidths and differences in their positions before and after x-ray diffraction measurements.

All data were collected, indexed, and integrated using CRYSALISPRO [version 1.171.43.67a (Rigaku Oxford Diffraction, 2023)], which also handled scaling and absorption. For the ambient data collection, a numerical absorption correction was performed using a face-based model of the crystal [16]. For high-pressure data, absorption was handled by an empirical correction using spherical harmonics, implemented in the SCALE3 ABSPACK scaling algorithm. The ambient structure was solved by SHELXT [17] while high-pressure data were solved using isomorphous replacement and all models further refined using SHELXL [17], with both stages performed in OLEX2 version 1.5-ac6-011 [18]. Complete crystallographic information (.cif) files, including embedded structure factors and SHELX refinement instructions (.res), are made available via the CCDC database, Deposition Nos. CCD 2302931_ 2302941.

C. Magnetometry

A radio-frequency (rf) susceptometry technique was used in which the sample is placed within a small detector coil of around 30 turns that forms the inductive part of an LCR circuit driven by a tunnel diode oscillator. Changes in the oscillation frequency (Act)) of the circuit are measured and related to the real part of the dynamic susceptibility,

$$\_\_= —7tf^{-'} \qquad (2)$$

where f is the filling factor of the detector coil [19—21].

Pressure dependent susceptometry was measured by placing the rf detector coil, containing a single crystal of $[Cu(pyz)_{0.5}(gly)]ClO_4$, in a piston-cylinder cell inserted in an 18 T superconducting magnet at the National High Magnetic Field Laboratory, Tallahasee, Florida. Additional measurements were taken at the University of Warwick using a pumped-^{3} He probe within the variable temperature insert of a 17 T superconducting magnet. The field was applied parallel to the [011] crystallographic direction. The pressure media used were glycerol (for x-ray diffraction measurements) and Daphne 7373 oil (for magnetometry), which give good hydrostatic pressure conditions under the pressures employed [22]. Values of pressure were determined in situ by tracking the pressure dependence of the fluorescence spectrum of a ruby chip located on the end of a fiber-optic cable situated next

to the sample. Measurements were made at 1.5, 2.6, 7.9, 13.1, 15.4, 18.1, 20.8, and 22 kbar with an uncertainty of 0.5 kbar estimated from the ruby fluorescence line widths.

D. Density functional theory

Spin-polarized DFT calculations were performed under the generalized gradient approximation (GGA) [23] using the plane wave pseudopotential code CASTEP [24]. Calculations were converged to 1 meV per atom using a plane wave cutoff of 1500 ev and a 5 x 5 x 3 k-point grid [25]. The experimentally determined unit cell was allowed to relax, since we were unable to realize the spin configurations required to extract coupling constants from the experimental cell. On permitting the unit cell to relax, the cell volume increases by approximately 25%. The increase is not uniform across

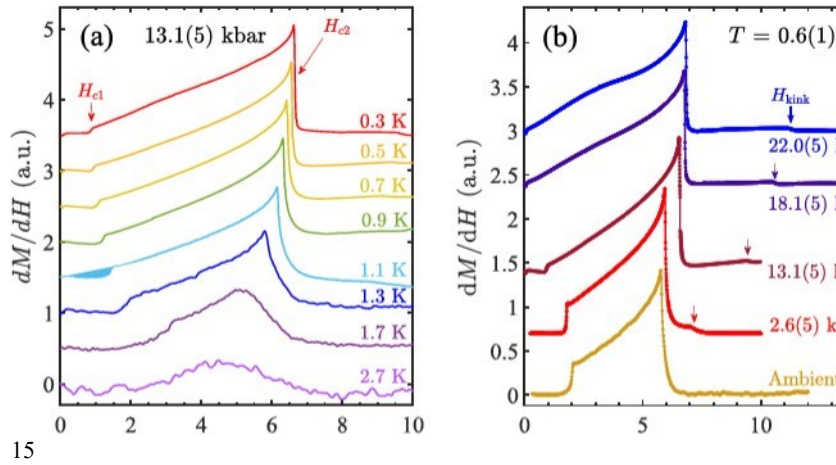

FIG. 3. (a) Field dependence of the dynamic susceptibility (dM/dH) measured at 13.1(5) kbar and various fixed temperatures for H Il [011]. (b) Pressure evolution of dM/dH at K. (Ambient-pressure data taken from Ref. [131.) (c) Pressure evolution of the magnetization M(H) measured at K determined by integrating the data in (b). The inset highlights the Hkink feature. The first critical field (Hcl), second critical field (Hc2), and kinklike feature (Hkink) are marked with arrows.

all unit cell directions; we find increases of 3.1%, 6.7%, and 16.9% in the a, b, and c directions, respectively, which is expected due to the different bonding mechanisms present in these different directions. Specifically, the properties of the covalent bonds that form the corrugated sheets of dimers are more easily captured using GGA DFT than the weaker interdimer bonds and this has the effect of increasing the interdimer spacing. Using this DFT-reIaxed cell, we find all of the spin configurations required to extract Jo and J'eff are stable solutions, whereas considering the experimental cell we find that the magnetism is greatly suppressed. We therefore use the DFT-relaxed structure as the starting point for all subsequent calculations. From the DFT-relaxed unit cell, a series of calculations were performed by applying pressure isotropically over a range of 0—60 kbar. Further details of the DFT calculations are found in the Appendix.

E. Quantum Monte Carlo calculations

The Stochastic Series Expansion (SSE) QMC algorithm was used to simulate Hamiltonian Eq. (1) on finite size systems. The SSE is a finite temperature QMC based on the stochastic sampling of the diagonal matrix elements of the density matrix expanded in a Taylor series using a suitable basis. An operator loop cluster update, in conjunction with a directed loop update, reduces the autocorrelation time for the system sizes studied here (up to spins) to a few Monte Carlo sweeps. It is known from earlier studies on weakly coupled Heisenberg chains that for spatially anisotropic systems, one needs to simulate rectangular lattices to obtain a monotonic system-size dependence of calculated physical observables for extrapolating to the thermodynamic limit—simulations of square lattices yield results that depend nonmonotonically on system size. Similar effects are expected for the present model and, accordingly, lattices with dimensions Lx x Lx x Lz were studied, where Lz is the dimension along the c axis. An aspect ratio of R Lx/Lz 2 was chosen for the finite-size lattice studies with 8 < la < 32. For each system size, an inverse temperature of ßJ0 = 8Lx was used to ensure that only the lowest energy state contributed to the calculated quantities. Estimates of the ground-state properties were obtained from simultaneous finite-size and finite-temperature extrapolation of results from simulations on finite-sized systems to the thermodynamic limit.

111. RESULTS

A. High-pressure magnetometry

Figure 3(a) shows an example data set, at a pressure of 13.1(5) kbar in this case, of the field dependence of the differential magnetization (dM/dH) for a single crystal of $[Cu(pyz)_{0.5}(gly)]ClO_4$measured at various temperatures using rf susceptometry. At the lowest measured temperature (T 0.3 K), two sharp cusps are seen in the data at '-ICI = 0.8 T and Hc2 6.7 T that correspond to the first critical field at which the singlet-triplet energy gap is closed, and a second critical field at which the spins are polarized along the field direction. Upon increasing temperature, Hcl and Hc2 move in closer proximity to each other and cease to be resolvable as separate features for temperatures in the range 1.7 < T <

2.7 K. This behavior is qualitatively similar to that seen at ambient pressure [13].

The pressure evolution of the dM/dH data measured at fixed temperatures of 0.6(1) K is shown in Fig. 3(b). Hcl and Hc2 are seen to shift to lower and higher fields, respectively, as pressure is applied. The cusp at Hcl is also diminished in size as it is pushed to lower fields. By 18.1(5) kbar and above, Hcl has dropped to zero field, while the more dramatic cusp at Hc2 rises to approximately 7 T. At p 2.6(5) kbar, an additional kink feature in dM/dH emerges above Hc2, marked in Fig. 3(b) by Hkink. This feature tracks to higher fields as pressure is increased up to the maximum value measured, 22.0(5) kbar, separating further from Hc2 at higher pressures.

By integrating the measured dM/dH responses in Fig. 3(b), one can extract the magnetization M(H) as shown in Fig. 3(c). At $p < 13.1(5)$ kbar, the form of M(H) remains

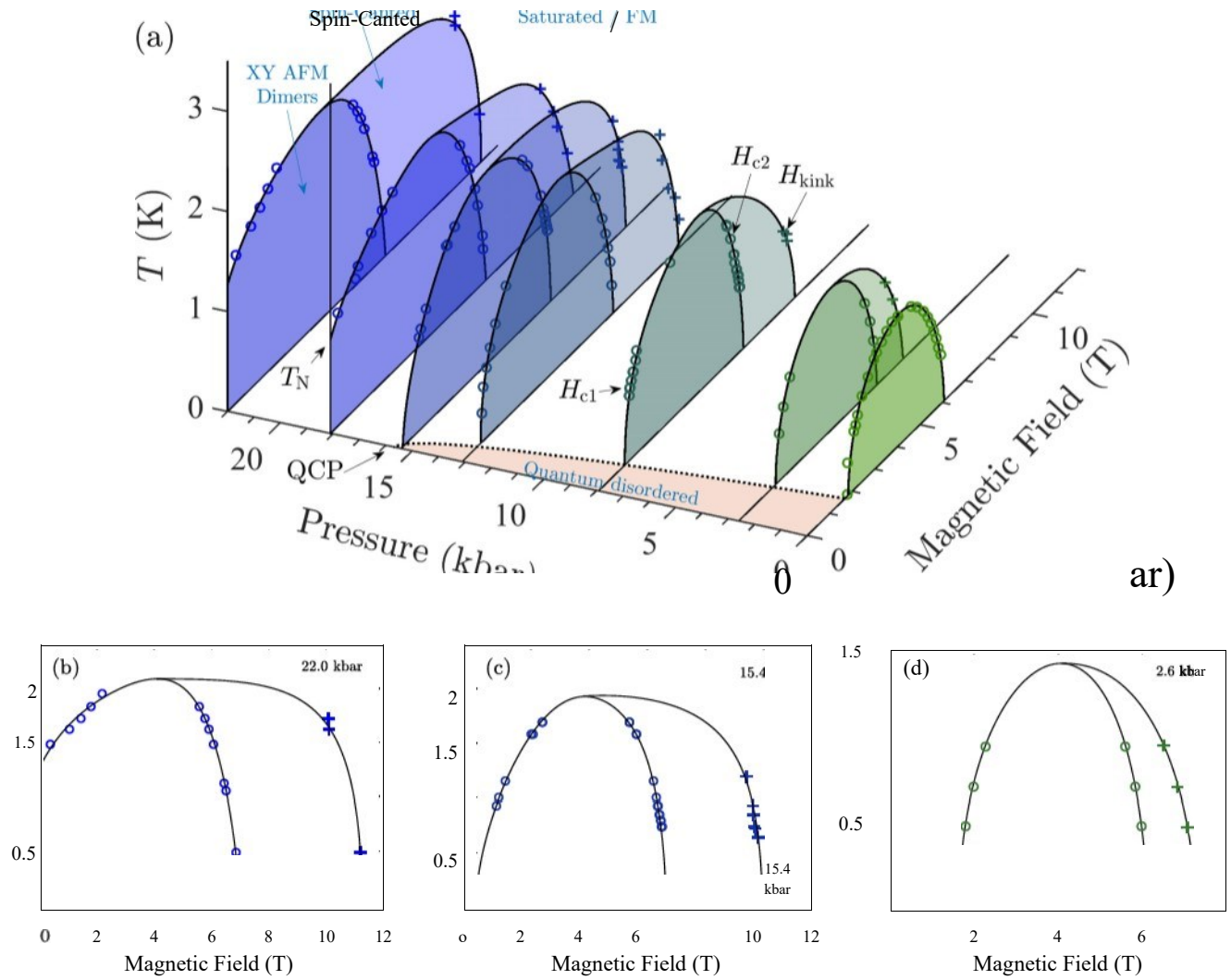

FIG. 4. (a) Pressure evolution of the H-T phase diagram for $[Cu(pyz)_{0.5}(gly)]ClO_4$ determined from the dM/dH data, a subset of which is shown in Fig. 3. Darker shaded areas denote regions of AFM order enclosed by Hel and Ho. Lighter shaded high-field regions enclosed by Ho and Hkink correspond to the likely spin-canted regime discussed in the text. Dotted line and orange shaded region indicates the area of quantum disorder in the p-H plane (shown again later in Fig. 8). The square-root phase boundary intersects the pressure axis at a 15.7(5) kbar QCP. At higher pressures the system orders in the absence of field with a finite Néel temperature TN as illustrated. (b)—(d) show the same 22.0, 15.4, and 2.6 kbar data plotted in (a), but on 2D plots for more clarity.

typical for a dimer system, with a sharp upturn due to the closing of the singlet-triplet energy gap and a plateau at Hc2 as the spins are nearly polarized along the field direction. For p 18.1(5) kbar, the abrupt low-field upturn in M(H) is lost as Hcl is driven to zero field, and M(H) rises with increasing gradient up to a sharp elbow at H Hc2. The data then rise more gradually before reaching saturation above H Hkink, best seen in the inset of Fig. 3(c).

Extracting the critical fields Hcl(T), Hc2(T) and Hkink(T) at each pressure enables the temperature—field phase diagram to be constructed and shown in Fig. 4. The ambient pressure dome of long-range X Y AFM order shown in green at ambient pressure changes in several ways as pressure is increased. First, the dome grows, Hcl shifts to lower values of field and Hc2 to higher, but the center of the dome does not show any marked shift. Such behavior is indicative of an increase in the interdimer exchange interactions with increasing pressure, with the intradimer interaction remaining largely unchanged.

This also explains the increase in the cutoff temperature at the top of the dome with applied pressure as an overall strengthening of the interdimer interactions leads to a stabilization of magnetic order to higher temperatures. Second, an additional high-field phase between Hc2 and Hkink emerges at finite pressures and grows in field range as pressure is increased. Third, Hcl is completely suppressed to zero field. The low-temperature values at each pressure are extrapolated to T 0 and the resulting data are fitted to a square-root phase boundary [8]. The fit describes the data well and is shown as the orange shaded region in the p-H plane of Fig. 4. In the absence of any signatures of first-order behavior or related changes in the phase diagram, we identify the presence of a QCP at a pressure of 15.7(5) kbar, which separates a highpressure region of zero-field magnetic order from a quantum disordered region at lower fields. Finally, the dome

develops a clear asymmetry, the origin of which is considered in the Discussion section below.

21(1) kbar. The twist angle of the pyrazine ring [Fig. 5(k)] also shows no change within errors upon increasing pressure. While

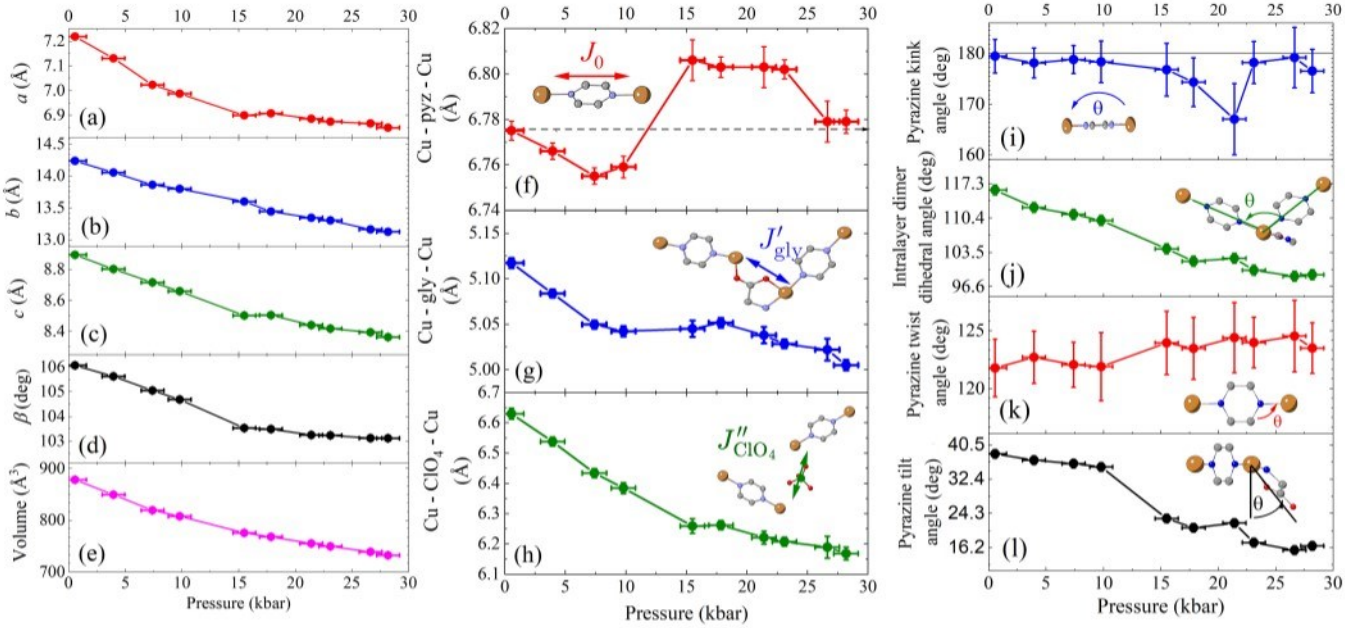

FIG. 5. Pressure dependencies of various aspects of the crystal structure of $[Cu(pyz)_{0.5}(gly)]ClO_4$: (a)–(e) the unit-cell parameters; (f)–(h) the distances between adjacent Cu(II) ions; and (i)–(l) bond angles along the exchange pathways. The intralayer dimer dihedral angle (j) is measured between the N–Cu–Cu–N atoms, and the pyrazine tilt angle (l) is the dihedral angle between O–Cu–N–C atoms. Insets show cartoons of the exchange pathway or bond-angle being considered. Measurements were performed at 300 K and errors are plotted at 30.

B. High-pressure crystallography

To account for the changes in the magnetic phase diagram, it is extremely useful to study the pressure evolution of the crystal structure. To this end, we carried out high-pressure single-crystal x-ray diffraction at room temperature, the results of which are displayed in Fig. 5. Figures 5(a)—5(e) show how the unit-cell parameters change with pressure. The results show no symmetry-breaking phase transition or notable abrupt structural rearrangements. The cell volume decreases linearly across the full range, while the ß angle decreases monotonically up to 10(1) kbar. Beyond 10(1) to 15(1) kbar, the rate of deformation decreases abruptly and the system becomes significantly more resistant to pressure. ß continues to decrease at a reduced rate up to the maximum pressure measured.

Figures 5(f)—5(l) highlight the effect of pressure upon various structural geometric parameters considered important to the magnetic exchange pathways. The data in Fig. 5(f) show that the intradimer exchange pathway (which dictates the size of JD is relatively unchanged over the measured pressure range, with a total variation of about 4-0.03 Å across the entire pressure range. This can be compared to order-of-magnitudes larger variation seen across similar distances for the interdimer Cu—Cu distances shown in Figs. 5(g) and 5(h) and discussed below. The change in kink angle of the bridging pyrazine molecule is shown in Fig. 5(i). A large kink can lead to an overlap of the d or dyz orbital of the Cu ion and the π orbital on the pyrazine ring [26], resulting in a exchange mechanism occurring alongside the a exchange mechanism [27] and increasing the overall exchange coupling in this direction. However, in our case the pyrazine molecule remains planar to a good degree of accuracy, with the exception of the point at the pyrazine ring is seen to tilt significantly toward the glycine ligand on increasing pressure [Fig. 5(1)], the pyrazine-tilt angle has been found to have little influence on the size of the magnetic exchange interactions in other Cu— pyz—Cu based low-dimensional magnets [28,291. Thus, the pyrazine ring is relatively robust over the measured pressure range, and so we expect the primary intradimer exchange to remain roughly constant.

Figure 5(g) shows that on increasing pressure, the distance between adjacent Cu ions along the interdimer Cu—gly—Cu direction initially decreases, plateaus in the pressure range $10 < P < 17$ kbar, then continues to decrease up to 28(1) kbar; a total reduction in the intralayer distance between Cu ions on adjacent dimers of 0.12 Å. This likely leads to an increase in the magnitude of the intralayer coupling (Jgly) between the dimers within the Q2D layers.

As shown in Fig. 5(h), the most dramatic change is seen in the interlayer distance, where dimers are coupled via C104 ions along the [101] direction. The interlayer Cu—Cu distance decreases linearly with increasing pressure up to 16 kbar, plateaus slightly up to 18 kbar, then continues to decrease up to 28 kbar. Over the measured pressure range, the interlayer distance between adjacent Cu ions is reduced by 0.5 Å. For simplicity, the data shown are the through-space distance, however, the atomic site separations along the expected interlayer exchange pathway show very similar behavior. This indicates the greatest effect pressure has on the system is to pack the dimer layers more tightly along the [101] direction, enhancing the interdimer exchange in this direction (J" ClO,) and causing adjacent dimers within the layers to become more orthogonal to each other [see Fig. 5(j)].

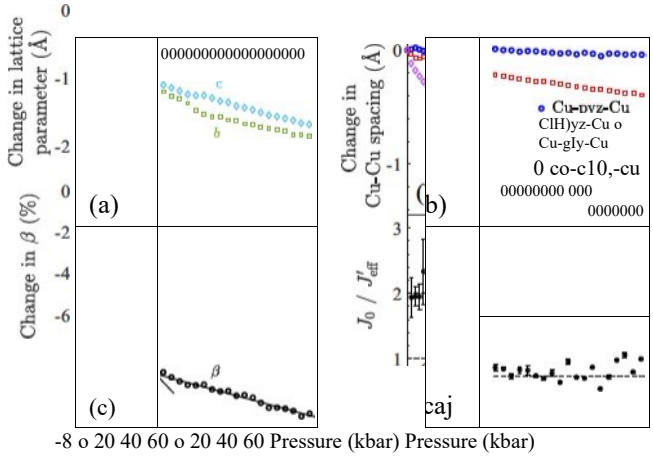

FIG. 6. DEI' results. (a) Theoretical evolution of lattice parameters of $[Cu(pyz)_{0.5}(gly)]ClO_4$ with simulated external pressure. (b) Change in the distance between Cu ions along the available exchange pathways. (c) Pressure dependence of the unit cell angle p; lines have been added as a guide to the eye. (d) Ratio of coupling constants Jo and J'eff across the calculated pressure range; dotted lines indicate the two distinct regimes.

The observed stiffening of the angle and associated features in the room-temperature crystal structure is likely caused by the elimination of the most accessible void space at low pressures, followed by harder deformations resulting from continued compression. Although the stiffening occurs between 10 and 15 kbar, it is unlikely to be directly linked to the QCP seen at 15.7(5) kbar in the low-temperature magnetometry data. As discussed in more detail below and supported by QMC calculations, the QCP is instead driven by the gradual evolution of the exchange energies across the entire pressure range.

C. Density functional theory

To better understand the effects of pressure on the exchange couplings, we performed spin-polarized DFT calculations by applying pressure isotropically over a range of 0—60 kbar as described in the Methods section. We find that the spin configuration with the lowest total energy, and therefore the ground-state magnetic structure, is AFM both within the Cu(ll) dimers and between the dimers. This is consistent with both the intradimer .10 and effective interdimer J'_{eff} =4(.J'1y + .18104) coupling constants being AFM.

The calculated effects of externally applied pressure on $[Cu(pyz)_{0.5}(gly)]ClO_4$ are shown in Fig. 6. All lattice parameters are predicted to decrease with applied pressure, with the decrease being continuous for a and c. However, there is a discontinuity in b at approximately 20 kbar [Fig. 6(a)]. It should be noted that the ambient-pressure unit cell calculated from DFT is approximately 25% larger than is realized experimentally. The discontinuity in b corresponds to a change in the unit cell angle ß, and while ß always decreases with increasing pressure, the rate of decrease is predicted to slow at around 20 kbar, as seen in Fig. 6(c). A change in the orientation of C104 molecules provides an explanation for the sudden changes in crystal structure seen by DFE at 20 kbar, with the C104 molecule undergoing a rotation at 20 kbar which allows for more efficient packing and the change in the b axis shown in Fig. 6(c). Cu—Cu distances are shown in Fig. 6(b), where it can be seen that the most dramatic changes are predicted to occur between the Cu ions in the exchange pathway mediated by C104 (J'é104), where the Cu—Cu distance is expected to decrease by approximately 1 Å with the application of 20 kbar. We note that the abrupt changes in behavior predicted by DEI' at 20 kbar are not observed in the experimental data up to 28(1) kbar. On this point, it is worth noting that the experimental results show evidence for a degree of lability and dynamic disorder in the position of the C104 anions that is not captured by I)Fr modeling and could explain any differences in the results between theory and experiment.

The effect of pressure on the exchange constants of $[Cu(pyz)_{0.5}(gly)]ClO_4$is also calculated and can be seen in Fig. 6(d). At all pressures, Jo and % are found to be positive, indicating that the magnetic interactions are AFM. There are two distinct regimes for the coupling constants as with the structural parameters, with the coupling strengths changing from those found at ambient pressure above 20 kbar. Across the full range of pressures, the coupling constant Jo remains quite stable around Jo = 8 K, with a small increase at the highest pressures to Jo 9 K. For the second coupling constant, J' , the behavior is more complex: in the region below 20 kbar the coupling is calculated to be roughly half the value of .10, and at higher pressures Jeff increases, such that the ratio J_0/J/eff I. In the region around the structural transition, the effect on the coupling constants is less clear, but the general trend shows that Jeff gets stronger with increasing pressure over a range of z 10 kbar to its final value above 20 kbar.

IV. DISCUSSION

A. The pressure-induced QCP

The x-ray diffraction experiments under applied pressure (Fig. 5) clearly indicate that the pyrazine molecules are robust to distortion, and the length of the Cu—pyz—Cu pathway, which mediates the primary intradimer exchange interaction (JD, remains roughly constant across the whole pressure range measured. The Cu—glycine—Cu distance changes relatively smoothly by approximately 0.1 Å on increasing the pressure to 28(1) kbar. At ambient pressure, it is this pathway that mediates the main interdimer interaction (J',), and an increase in this exchange energy is therefore expected as pressure is applied. However, the largest change in the lattice occurs in the interlayer separation along c. This causes the Cu—C104Æu distance [Fig. 5(h)] to reduce by close to 0.5 Å by the maximum applied pressure. Thus, it is reasonable to assume that the interlayer exchange strength J" C104' which was previously found to be negligible compared to Jo and J' gly at ambient pressure [13], is the interaction that is most decisive in determining the behavior of the system under pressure.

This conclusion is supported by our DFT calculations (Fig. 6), which predict that the Cu—C104—Cu distance should decrease significantly under pressure, while the Cu—glycine—Cu pathway is much less compressed, and the Cu—pyz—Cu is the most robust to change. The calculations show further that the effective interdimer coupling, the sum of all interdimer

exchange strengths, doubles relative to the intradimer coupling across 30 kbar of applied pressure. Although this result

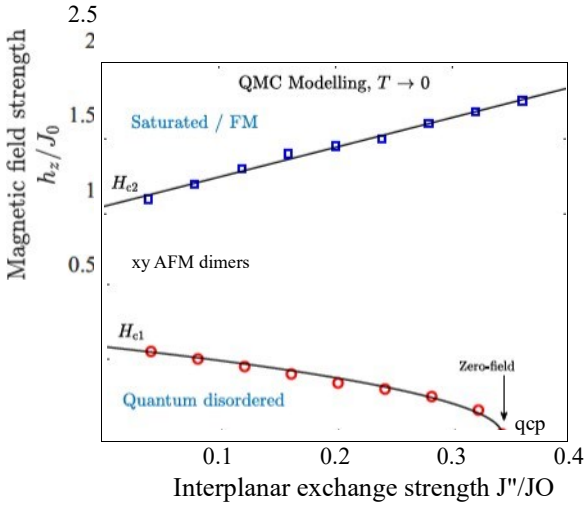

FIG. 7. Critical fields predicted from quantum Monte Carlo calculations as a function of changing the interplanar interdimer interaction. The ratio of in-plane inter- and intradimer exchange J'/JO is set to 0.276, the value determined experimentally at ambient pressure [13]. The box size used was N = 16 x 16 x 8. As argued in the text, the effect of pressure can be primarily linked to an increase in J" , and so these calculations can be compared to the experimental field-pressure phase diagram of Fig. 8.

is influenced by the quite abrupt change predicted to occur in the b-axis lattice parameter at 20 kbar (which is not seen in the experimental data), the reduction in interlayer distance clearly plays a key role.

To confirm the origin of the zero-field ordered state, QMC calculations were also performed as outlined in the Methods section. The results shown in Fig. 7 indicate that , the critical field that separates XY order from the quantum disordered phase, can be pushed to zero by an increase from 0 to 0.34 in the Jå04/Jo ratio when J'l is fixed at its experimentally determined ambient-pressure value. This would suggest that the simplest explanation for the observed QCP at 15.7(5) kbar and the associated onset of zero-field magnetic order is the increase under pressure of the size of the interlayer interdimer coupling mediated through the perchlorate molecules, which in turn is driven by the anisotropic compression of the crystal lattice. Previous heat-capacity measurements have shown that the magnetic properties of $[Cu(pyz)_{0.5}(gly)]ClO_4$ are highly two-dimensional at ambient pressure [13]. Our present results therefore imply that the primary driver of the zero-field magnetic order is a dimensional crossover from Q2D to threedimensional magnetism. The Q2D spin-1/2 dimer material PHCC also shows a pressure-induced QCP. There the effect of pressure is to weaken the intradimer coupling and push the dome of magnetic order to lower fields [30], which is different from the broadening of the dome we observe in our material.

B. Quantum fluctuations and asymmetry in the phase diagram

The magnetometry measurements point to a somewhat more complicated situation than the simple picture above. Figure 8 shows how the three critical fields observed in the dynamic susceptibility measurements evolve as a function of pressure. Hcl is the position of the lower-field cusp in the

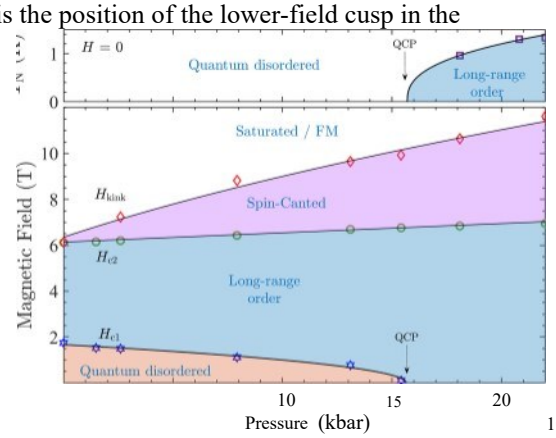

FIG. 8. Lower panel: p-H phase diagram at low temperature, extrapolated from the data shown in Fig. 4. Hel is suppressed to zero-field and zero-temperature at pc = 15.7(5) kbar. Upper panel: pressure evolution of the zero-field dimer ordering temperature TN at pressures above pc. Solid lines are guides to the eye.

susceptibility or the point at which the magnetization begins to rise quickly with field (see Fig. 3). It marks the transition between the quantum-disordered dimer phase and the XYordered state and is suppressed by initial pressurization at a constant rate of —71 (4) mT/kbar up to 13 kbar, after which it drops abruptly to the QCP at 15.7(5) kbar.

The field Hc2 is the location of the large cusp in susceptibility, which marks the point at which the magnetization begins to plateau. At ambient pressure, this corresponds to the transition between the X Y ordered state and the field-saturated phase, where the Zeeman energy surpasses the sum of all the AFM interactions between the spins. As pressure is applied, Hc2 rises linearly at 40(1) mT/kbar, which is notably slower than the pressure-induced drop in I-ICI.

That Hel and 1--1c2 vary with pressure at different rates is not straightforward to understand. It has previously been noted that the effect of quantum fluctuations is greater on the lowercritical-field transition, where the bosonic effective mass is strongly renormalized, than for the transition at Hc2 [13]. This is manifested by a strong asymmetry in the entropy change seen at the two transitions as measured using heat capacity [13]. It has been predicted that the disparity in the sizes of the peaks in heat capacity at the two transitions should increase strongly as Hc1/Hc2 decreases, diverging as this ratio tends to zero [31]. This effect is clearly reflected in the sizes of the features seen at the two field-induced transitions in our susceptibility data, as shown in Fig. 3(b). As the pressure increases, the size of the feature at Hcl diminishes quickly, indicating that the renormalization due to quantum fluctuations gets significantly stronger as this transition is pushed to lower fields. Finally, as the pressure-induced QCP is approached, the feature at Hcl disappears altogether, in keeping with the predictions of Ref. [31].

In principle, the variation in the relative importance of quantum fluctuations at the two transitions could also explain their different shifts as a function of pressure. However, the QMC calculations are also sensitive to effects of quantum

fluctuations and the results show the two transitions evolving at very similar rates.

This points to an unconventional asymmetry in the phase diagram beyond that which might be expected from the effect of quantum fluctuations alone. A possible explanation could arise if the size of the effective interlayer coupling depends on the component of the spins perpendicular to the c axis. This would lend a field dependence to the interdimer exchange strength, which would diminish as the spins become more aligned with c. Our magnetometry measurements were performed with H Il [01 Il and so, if this proposition has merit, then the interlayer coupling would become less effective with increasing field and hence the transition at Hel would feel the pressure-induced enhancement of Jé104 more strongly than the Hc2 transition, giving rise to the observed difference in pressure evolution of the two transitions.

C. High-field phase and the DM interaction

In addition to Hel and Hc2, for pressures above ambient, another higher-field feature is seen at Hkink, marking a very small step in magnetization [as shown in the inset to Fig. 3(c)]. Assuming that it arises from the bulk behavior of the system, this feature suggests that, for elevated pressures, the spins in the state above Hc2 are canted slightly from the field direction, and fully align parallel to H only for H > Hkink. Such a canting is typically caused by energy scales in the spin Hamiltonian, such as anisotropy, that compete with the Zeeman term. The size of the step in magnetization that occurs at Hkink increases with pressure, and at 23 kbar is approximately 2% of the saturated moment. Assuming all spins are canted at the same angle from the field, this would correspond to a canting angle of about 11.5^0 . The crossover field Hkink itself increases rapidly with pressure at a rate of 230(10) mT/kbar, which is significantly faster than the changes in either Hcl or He.

The noncentrosymmetric structure of $[Cu(pyz)_{0.5}(gly)]ClO_4$, with its alternating orientation of dimers within the ab plane, allows for the existence of an antisymmetric DM interaction between spins, which is known to give rise to canted spin structures. No evidence for the effect of such an interaction was forthcoming in the previous ambient pressure studies of this system. (DM interactions result from a second-order correction to the energy arising from the combination of spin-orbit interaction and exchange, so are expected to be smaller than Zeeman, single-ion anisotropy or exchange effects). However, as can be seen from Fig. 5(j), our x-ray data suggest that the dihedral angle between adjacent dimers in the corrugated planes sharpens from $116.0(8)^0$ at ambient pressure to $99.0(9)^0$ by 28(1) kbar, potentially increasing the strength of the DM interaction, and thus providing an explanation for the enhancement of the canting angle and the field Hkink as pressure grows.

We might expect any DM interaction present to influence the transition at Hcl as well as that at Hc2. Indeed, the energetic contribution from the DM interaction should diminish quickly with increasing applied field as the relative angle between neighboring spins is reduced, and so the perturbation to the 1--lamiltonian from DM is likely larger in the low-field limit. Exactly how this Hcl transition between quantum-disordered and XY-ordered states would be affected by a DM term is hard to anticipate without detailed calculations and a better knowledge of the direction and size of the dominant DM vector. However, the combination of DM and the field-dependent interlayer coupling proposed above would seem to provide the most plausible explanation for the small realignment of the spins at Hkink, as well as the asymmetry between low-field and high-field transitions via an intrinsic, bulk mechanism, without invoking some local effect.

V. SUMMARY

Given the discussion above, it seems clear that the interlayer exchange term increases strongly with pressure and probably drives the quantum phase transition observed in the magnetometry data at 15.7(5) kbar. Nevertheless, accounting for the pressure dependence of all of the features seen in the susceptibility of $[Cu(pyz)_{0.5}(gly)]ClO_4$ is not trivial. The observed results likely arise from both symmetric and antisymmetric interaction terms in the Hamiltonian, and a field dependence in one or more of these interactions is possible. Inelastic neutron scattering would help shed further light on exactly what drives the phase transitions and efforts are underway to grow sufficiently sized deuterated crystals to enable these measurements. With its experimentally accessible exchange energies, this is one of very few S = 1/2 dimer materials on which neutron scattering studies could be performed across both field-induced QCPs. In the meantime, it is apparent that the molecular bridges that connect the spins in this class of material support an interesting hierarchy of competing energy scales. Furthermore, the resulting crystal structure undergoes anisotropic compression on application of pressure and the balance of these interactions seems to evolve in a nontrivial manner both in pressure and magnetic field.

Data presented in this paper will be made available at [32]. Complete crystallographic information (.cif) files, including embedded structure factors and SHELX refinement instructions (.res), are made available via the CCDC, Deposition Nos. CCD 2302931-2302941.

ACKNOWLEDGMENTS

We are indebted to J.L. Manson, now deceased, for instigating this work, for his role in designing and growing the samples, and for many other invaluable contributions. We thank T. Orton and P. Ruddy for technical assistance. This project has received funding from the European Research Council (ERC) under the European Union's Horizon 2020 research and innovation program (Grant Agreement No. 681260). Crystallographic data were collected using an instrument that received funding from the European Research Council (ERC) under the European Union's Horizon 2020 research and innovation program (Grant Agreement No. 637313). A portion of this work was performed at the National High Magnetic Field Laboratory, which is supported by National Science Foundation Cooperative Agreement No. DMR-1644779 and the State of Florida. We acknowledge the support of EPSRC (UK) (Grant No. EP/N032128/1) and Durham Hamilton HPC. This work used the ARCHER2 UK

National Supercomputing Service [33] (Grant No. EP/X035891/1).

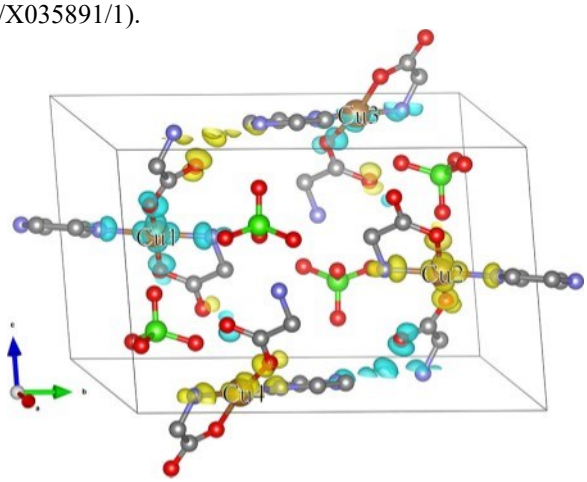

FIG. 9. Spin density of the antiferromagnetic ground state of $[Cu(pyz)_{0.5}(gly)]ClO_4$. Labels on the Cu ions refer to the order of ions considered in each different spin configuration. H atoms have been removed for clarity.

APPENDIX: DETAILS OF DENSITY FUNCTIONAL THEORY CALCULATIONS

To calculate the coupling constants, a single unit cell containing four Cu(ll) ions was used, which allows for a maximum of eight unique magnetic configurations. Using a single unit cell then allows us to extract Jo and J'eff, where J'eff = 4(J'pyz + J''_{ClO_4}).

A supercell would be required to extract all three coupling constants, however, this would be prohibitively large computationally. For each pressure, calculations were performed by initializing seven different spin configurations and calculating

TABLE I. Energies of configurations of spins in $[Cu(pyz)_{0.5}(gly)]ClO_4$.

Spin configuration	Energy
↑↓↑↑	E_0
↑↓↓↑	$2J_0 + J'_{\text{eff}} + E_0$
↑↓↓↓	E_0
↑↑↓↑	E_0
↑↑↑↓	E_0
↑↓↑↓	$2J_0 - J'_{\text{eff}} + E_0$
↑↑↓↓	$-2J_0 + J'_{\text{eff}} + E_0$

the total energy of each. These total energies are then used to solve a set of simultaneous equations [34] in terms of Jo and J'eff.

As the calculations provide an overcomplete set, spin configurations that are equivalent in our model can be used to estimate the uncertainty in the couplings.

Figure 9 shows isosurfaces of the ground-state spin density in $Cu(pyz)_{0.5}(gly)]ClO_4$. There is significant spin density on each of the Cu(ll) ions with neighboring ions having opposite signs. In each case, the Cu(ll) ions induce spin density on the O atoms in the glycine ligands and the N atoms in pyrazine. Table I shows the system of equations used to evaluate the exchange couplings in $Cu(pyz)_{0.5}(gly)]ClO_4$. The states are represented by the direction of the magnetic moment on each Cu ion in the order Cul, Cu2, Cu3, Cu4, as given in Fig. 9. Each equation in the system contains the total energy of the system, excluding magnetic exchange effects, Eo•, in many of the spin configurations the contributions to Jo and J'eff effectively cancel, leaving only the contribution from Eo.

[l] Y. Uchiyama, Y. Sasago, I. Tsukada, K. Uchinokura, A. Zheludev, T. Hayashi, N. Miura, and P. Böni, Spin-vacancyinduced long-range order in a new Haldane-gap antiferromagnet, Phys. Rev. Leu. 83, 632 (1999).

[2] T. Radu, H. Wilhelm, V. Yushankhai, D. Kovrizhin, R. Coldea, Z. Tylczynski, T. Lühmann, and F. Steglich, Bose-Einstein condensation of magnons in Cs2CuC14, Phys. Rev. Lett. 95, 127202 (2005).

[3] V. S. Zapf, D. zocco, B. R. Hansen, M. Jaime, N. Harrison, C. D. Batista, M. Kenzelmann, C. Niedermayer, A. Lacerda, and A. Paduan-Filho, Bose-Einstein condensation of S — 1 nickel spin degrees of freedom in $NiCl_2$-$4SC(NH_2)_2$,Phys. Rev. Lett. 96, 077204 (2006).

[4] R. Coldea, D. A. Tennant, E. M. Wheeler, E. Wawrzynska, D. Prabhakaran, M. Telling, K. Habicht, P. Smeibidl, and K. Kiefer, Quantum criticality in an Ising chain: Experimental evidence for emergent E8 symmetry, Science 327, 177 (2010).

[5] S. Sachdev and B. Keimer, Quantum criticality, Phys. Today 64(2), 29 (2011).

[6] V. Zapf, M. Jaime, and C. D. Batista, Bose-Einstein condensation in quantum magnets, Rev. Mod. Phys. 86, 563 (2014).

[7] C. Rüegg, B. Normand, M. Matsumoto, A. Furrer, D. F. McMorrow, K. W. Krämer, H. U. Güdel, S. N. Gvasaliya, H. Mutka, and M. Boehm, Quantum magnets under pressure: Controlling elementary excitations in TICuC13, Phys. Rev. Lett. 100, 205701 (2008).

[8] C. Rüegg, A. Furrer, D. Sheptyakov, T. Strässle, K. W. Krämer, H.-U. Güdel, and L. Mélési, Pressure-induced quantum phase transition in the spin-liquid TICuC13, Phys. Rev. Lett. 93, 257201 (2004).

[9] K. Goto, M. Fujisawa, H. Tanaka, Y. Uwatoko, A. Oosawa, T. Osakabe, and K. Kakurai, Pressure-induced magnetic quantum phase transition in gapped spin system KCuC13, J. Phys. Soc. Jpn. 75, 064703 (2006).

[10] M. Thede, A. Mannig, M. Månsson, D. Hüvonen, R. Khasanov, E. Morenzoni, and A. Zheludev, Pressure-induced quantum critical and multicritical points in a frustrated spin liquid, Phys. Rev. Lett. 112, 087204 (2014).

[11] S. Bettler, G. Simutis, G. Perren, D. Blosser, S. Gvasaliya, and A. Zheludev, High-pressure Raman study of the quantum magnet (C4H12N2)Cu2C16, Phys. Rev. B 96, 174431 (2017).

[12] T. Lancaster, P. A. Goddard, S. J. Blundell, F. R. Foronda, S. Ghannadzadeh, J. S. Möller, P. J. Baker, F. L. Pratt, C. Baines, L. Huang, J. Wosnitza, R. D. McDonald, K. A. Modic, J. Singleton, C. V. Topping, T. A. W. Beale, F. Xiao, J. A. Schlueter, A. M. Barton, R. D. Cabrera, K. E. Carreiro, H. E. Tran, and J. L. Manson, Controlling magnetic order and quantum disorder in molecule-based magnets, Phys. Rev. Lett. 112, 207201 (2014).

[13] J. Brambleby, P. A. Goddard, J. Singleton, M. Jaime, T. Lancaster, L. Huang, J. Wosnitza, C. V. Topping, K. E. Carreiro, H. E. Tran, Z. E. Manson, and J. L. Manson, Adiabatic physics of an exchange-coupled spin-dimer system: Magnetocaloric effect, zero-point fluctuations, and possible two-dimensional universal behavior, Phys. Rev. B 95, 024404 (2017).

[14] T. Lancaster, F. Xiao, B. M. Huddart, R. C. Williams, F. L. Pratt, S. J. Blundell, S. J. Clark, R. Scheuermann, T. Goko, S. Ward, J. L. Manson, C. Rüegg, and K. W. Krämer, Quantum magnetism in molecular spin ladders probed with muon-spin spectroscopy, New J. Phys. 20, 103002 (2018).

[15] H. Mao, J. Xu, and P. Bell, Calibration of the ruby pressure gauge to 800 kbar under quasi-hydrostatic conditions, J. Geophys. Res. 91, 4673 (1986).

[16] R. C. Clark and J. S. Reid, The analytical calculation of absorption in multifaceted crystals, Acta Cryst. A 51, 887 (1995).

[17] G. M. Sheldrick, Crystal structure refinement with SHELXL, Acta cryst. C 71, 3 (2015).

[18] O. V. Dolomanov, L. J. Bourhis, R. J. Gildea, J. A. K. Howard, and H. Puschmann, OLEX2: A complete structure solution, refinement and analysis program, J. Appl. Cryst. 42, 339 (2009).

[19] R. B. Clover and W. P. Wolf, Magnetic susceptibility measurements with a tunnel diode oscillator, Rev. Sci. Instrum. 41, 617 (1970).

[20] T. Coffey, Z. Bayindir, J. F. Decarolis, M. Bennett, G. Esper, and C. C. Agosta, Measuring radio frequency properties of materials in pulsed magnetic fields with a tunnel diode oscillator, Rev. Sci. Instrum. 71, 4600 (2000).

[21] S. Ghannadzadeh, M. Coak, I. Franke, P. Goddard, J. Singleton, and J. Manson, Measurement of magnetic susceptibility in pulsed magnetic fields using a proximity detector oscillator, Rev. Sci. Instrum. 82, 113902 (2011).

[22] S. Klotz, J.-C. Chervin, P. Munsch, and G. Le Marchand, Hydrostatic limits of 11 pressure transmitting media, J. Phys. D: Appl. Phys. 42, 075413 (2009).

[23] J. P. Perdew, K. Burke, and M. Ernzerhof, Generalized gradient approximation made simple, Phys. Rev. Lett. 77, 3865 (1996).

[24] S. J. Clark, M. D. segall, C. J. Pickard, P. J. Hasnip, M. 1. Probert, K. Refson, and M. C. Payne, First principles methods using CASTEP, Z. Kristallogr. cryst. Mater. 220, 567 (2005).

[25] H. J. Monkhorst and J. D. Pack, Special points for Brillouinzone integrations, Phys. Rev. B 13, 5188 (1976).

[26] R. T. Butcher, Metal-organic copper(ll) complexes: An investigation of exchange coupled ladders, rectangles, and square magnetic systems, Ph.D. thesis, Clark University, 2008.

[27] L. H. Dos Santos, A. Lanza, A. M. Barton, J. Brambleby, W. J. Blackmore, P. A. Goddard, F. Xiao, R. C. Williams, T. Lancaster, F. L. Pratt, S. J. Blundell, J. Singleton, J. L. Manson, and P. Macchi, Experimental and theoretical electron density analysis of copper pyrazine nitrate quasi-low-dimensional quantum magnets, J. Am. Chem. Soc. 138, 2280 (2016).

[28] S. Vela, J. Jornet-Somoza, M. M. Turnbull, R. Feyerherm, J. J. Novoa, and M. Deumal, Dividing the spoils: Role of pyrazine ligands and perchlorate counterions in the magnetic properties of Bis(pyrazine)diperchloratecopper(II), $[Cu(pz)_2](ClO_4$ h, Inorg. Chem. 52, 12923 (2013).

[29] E. P Kenny, A. C. Jacko, and B. J. Powell, Tight-binding approach to Pyrazine-Mediated superexchange in CopperPyrazine antiferromagnets, Inorg. Chem. 60, 11907 (2021).

[30] G. Perren, J. S. Möller, D. Hüvonen, A. A. Podlesnyak, and A. Zheludev, Spin dynamics in pressure-induced magnetically ordered phases in (C4H12N2)Cu2C16, Phys. Rev. B 92, 054413 (2015).

[31] Y. Kohama, A. V. Sologubenko, N. R. Dilley, V. S. Zapf, M. Jaime, J. A. Mydosh, A. Paduan-Filho, K. A. AlHassanieh, P. Sengupta, S. Gangadharaiah, A. L. Chernyshev, and C. D. Batista, Thermal transport and strong mass renormalization in NiC124SC(NH2h, Phys. Rev. Leu. 106, 037203 (2011).

[32] wrap.warwick.ac.uW180953.

[33] https://www.archer2.ac.uk.

[34] I. O. Thomas, S. J. Clark, and T. Lancaster, Exchange constants in molecule-based magnets derived from density functional methods, Phys. Rev. B 96, 094403 (2017).